

Nanophotonic Materials for Twisted-Light Manipulation

Haoran Ren* and Stefan A. Maier*

Twisted light, an unbounded set of helical spatial modes carrying orbital angular momentum (OAM), offers not only fundamental new insights into structured light–matter interactions, but also a new degree of freedom to boost optical and quantum information capacity. However, current OAM experiments still rely on bulky, expensive, and slow-response diffractive or refractive optical elements, hindering today's OAM systems to be largely deployed. In the last decade, nanophotonics has transformed the photonic design and unveiled a diverse range of compact and multifunctional nanophotonic devices harnessing the generation and detection of OAM modes. Recent metasurface devices developed for OAM generation in both real and momentum space, presenting design principle and exemplary devices, are summarized. Moreover, recent development of whispering-gallery-mode-based passive and tunable microcavities, capable of extracting degenerate OAM modes for on-chip vortex emission and lasing, is summarized. In addition, the design principle of different plasmonic devices and photodetectors recently developed for on-chip OAM detection is discussed. Current challenges faced by the nanophotonic field for twisted-light manipulation and future advances to meet these challenges are further discussed. It is believed that twisted-light manipulation in nanophotonics will continue to make significant impact on future development of ultracompact, ultrahigh-capacity, and ultrahigh-speed OAM systems-on-a-chip.

1. Introduction

The development of miniaturized photonic devices to generate, transmit, manipulate, and retrieve increasingly enormous amounts of data for high-capacity optical networks is vitally important. During the 1980s, optical communication experiments driven by wavelength-division multiplexing were performed on large optical tables using expensive devices that were not meant for practical communication systems. The development of cost-effective, integrated devices then followed, to enable wavelength-division multiplexing to be widely deployed. However, present-day optical communication systems using wavelength-division multiplexing are heading toward a capacity limit (Figure 1A). To further scale-up the capacity of photonic devices, twisted light multiplexing, based on an unbounded set of orbital angular momentum (OAM) modes, has been recognized as a viable space-division multiplexing approach to significantly increasing the multiplexing capacity of future optical communication systems.^[1] In this context, OAM multi-

plexing has been employed for optical communications in free space,^[2,3] optical fibers,^[4] and quantum communications.^[5–7] It should be mentioned, however, OAM modes are only a subset of the Laguerre–Gaussian modes of structured light,^[8] and increasing optical multiplexing capacity can also be realized from other sets of orthogonal spatial modes.^[9] However, owing to the fast growing OAM research field, a broad range of photonic devices used for the OAM generation, multiplexing, detection, and demultiplexing have been developed, offering the OAM a compelling advantage to be largely deployed in future photonic information systems.

The angular momentum is a property to describe the rotation of an object around an axis. When it applies to light beams, the angular momentum \mathbf{L} can be defined as the cross-product between the position vector \mathbf{r} and the linear momentum vector


$$\mathbf{L} = \epsilon_0 \int \mathbf{r} \times (\mathbf{E} \times \mathbf{B}) d^3r \quad (1)$$

where ϵ_0 is the vacuum permittivity, \mathbf{E} and \mathbf{B} are the vectorial electric and magnetic fields of an electromagnetic wave. The angular momentum can be separated in the paraxial limit into two parts: the spin angular momentum (SAM) associated with circular polarization, and the OAM manifested by an optical vortex beam with a helical wavefront.^[10] For both paraxial and

H. Ren
MQ Photonics Research Centre
Department of Physics and Astronomy
Macquarie University
Macquarie Park, NSW 2109, Australia
E-mail: haoran.ren@mq.edu.au

S. A. Maier
Chair in Hybrid Nanosystems
Nanoinstitute Munich
Faculty of Physics
Ludwig-Maximilians-University Munich
80539 Munich, Germany
E-mail: stefan.maier@physik.uni-muenchen.de

S. A. Maier
Department of Physics
Imperial College London
London SW7 2AZ, UK

 The ORCID identification number(s) for the author(s) of this article can be found under <https://doi.org/10.1002/adma.202106692>.

© 2022 The Authors. Advanced Materials published by Wiley-VCH GmbH. This is an open access article under the terms of the Creative Commons Attribution License, which permits use, distribution and reproduction in any medium, provided the original work is properly cited.

DOI: 10.1002/adma.202106692

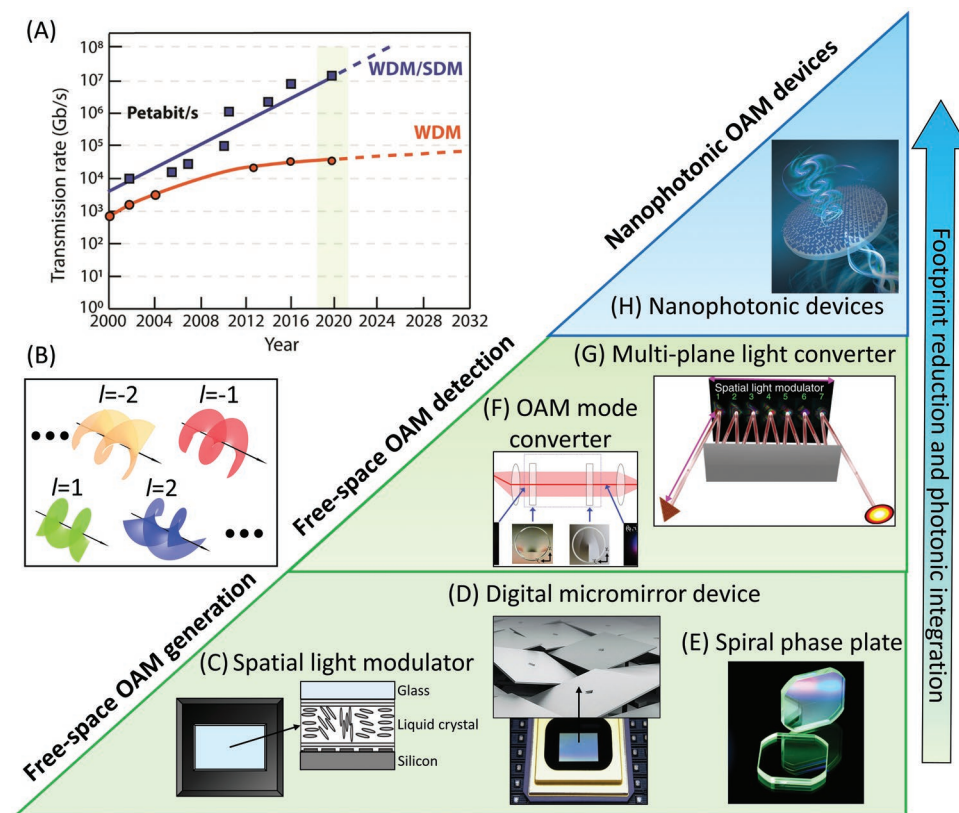


Figure 1. Roadmap of photonic devices for twisted-light manipulation and motivation of nanophotonic integration. A) Evolution of transmission capacity of fiber-optic communication systems. B) Schematic of the OAM of light carried by a helical wavefront. C–E) Conventional free-space OAM generation based on spatial light modulators (C), digital micromirror devices (D), and spiral phase plates (E). F, G) Conventional free-space OAM detection based on an OAM mode converter (F) and a multiple-plane light converter (G). H) Nanophotonic manipulation of OAM of light allows footprint reduction and photonic integration for on-chip OAM applications. WDM: wavelength-division multiplexing. SDM: space-division multiplexing that harnesses the OAM multiplexing. Image for (D): Reproduced with permission, copyright Norx AS. Image for (E): Reproduced with permission.^[104] Copyright Vortex Photonics. Image for (F): Reproduced with permission.^[105] Copyright 2014, Springer Nature. Image for (G): Reproduced under the terms of the CC-BY Creative Commons Attribution 4.0 International license (<https://creativecommons.org/licenses/by/4.0>).^[19] Copyright 2019, The Authors, published by Springer Nature.

nonparaxial beams (e.g., a tightly focused beam and near-field optics), the total angular momentum

$$J = (\sigma + l)\hbar \quad (2)$$

is a conserved quantity, where the SAM carries two possible states $\sigma = \pm 1$ per photon, and the OAM, $l\hbar$ per photon, can take any integer value l in $[-\infty, \infty]$ (where \hbar is the Planck's constant h divided by 2π). This total angular momentum conservation law underpins the photonic spin-to-orbital angular momentum conversion.^[11]

Unlike the SAM related to the polarization helicity, light also carries OAM in its wavefront in both intrinsic and extrinsic terms and the latter is coordinate-dependent.^[12] The intrinsic OAM, hereafter simply named as OAM, is carried by a helical wavefront that has a phase twist along the azimuthal direction in the transverse plane of an optical beam. In 1992, Allen et al. pioneered the discovery of the OAM in an optical vortex beam,^[13] with a helical phase distribution that mathematically satisfies $\exp(il\varphi)$, where l is the azimuthal mode index and φ is the azimuthal angle of an OAM beam, respectively. Strikingly,

the OAM degree of freedom has a theoretically unbounded set of eigenstates $\pm l\hbar$, where the integer number l determines how strong the wavefront is azimuthally twisted (Figure 1B). All OAM eigenstates are mutually orthogonal, opening the possibility of using OAM modes as independent information channels to carry optical information with negligible crosstalk.

However, current OAM experiments inevitably use bulky, expensive, and slow spatial light modulators (SLMs) (Figure 1C) or digital micromirror devices (DMDs) (Figure 1D) to generate and detect OAM modes. More critically, the free-space processing of OAM-multiplexing information via SLMs generally incurs undesired modal coupling caused by turbulence and turbidity, large beam divergence, and misalignment between the OAM transmitter and receiver, which represent key challenges facing today's OAM-multiplexing systems. While DMDs are faster ($\approx 10 \mu\text{s}$), they typically offer lower resolution, as each micromirror forms a pixel. Although spiral phase plates (Figure 1E) could offer a high spatial resolution led to the generation of higher OAM orders up to 10 010,^[14] the bulky phase plates cannot be used for photonic integration and the cost of fabrication is very high.

Even though the use of a SLM, a DMD, or a spiral phase plate can realize the OAM detection, it can detect only one OAM mode at a time (typical SLM or DMD devices have a much slower response (≈ 1 kHz) to process high data rate (≈ 10 Gb s⁻¹) telecommunication signals) and simultaneous detection of multiple OAM modes demands the multiple use of these optical elements with a power-splitting setup.^[1–4] To achieve more efficient OAM detection in free space, log-polar mode converters^[15–18] (Figure 1F) and multiplane light converters^[19] (Figure 1G) are used that use multiple phase elements to convert and map the OAM phase into distinct lateral positions, without sacrificing the power in each OAM mode. However, these methods typically rely on a large optical path (e.g., >100 mm@1.55 μ m) to perform the conformal transformation and mapping of OAM modes. It is worthwhile mentioning that a compact log-polar mode converter has recently been demonstrated, although it relies on a large optical path and a free-space beamsplitter to implement the OAM detection and demultiplexing.^[20]

As was the case for wavelength-division multiplexing in optical communications earlier, the future of OAM deployment would greatly benefit from photonic integration of OAM devices and systems (e.g., transmitters, multiplexers, demultiplexers, and receivers). Nanophotonics has opened the door to device miniaturization, leading to a diverse range of compact and multifunctional optical devices harnessing the generation and detection of optical vortices (Figure 1H), such as plasmonic and dielectric OAM metasurfaces in both real^[21–24] and momentum space,^[25–30] vortex microemitters,^[31] vortex micro-lasers,^[32–34] single-photon vortex emitter,^[35] plasmonic vortex generators,^[36,37] plasmonics-based OAM detectors,^[17,38–43] and OAM photodetectors.^[44] Here, we provide a comprehensive overview of nanophotonic devices and materials for the OAM generation and detection and discuss key challenges and new opportunities for these devices to be widely deployed.

2. Metasurface Generation of OAM in Real Space

2.1. Plasmonic Metasurfaces

In nanophotonics, both plasmonic and dielectric materials driven by different physics have recently been developed for compact OAM generation in real space. Since a helical wavefront that carries the OAM can be imprinted by a phase-only metasurface, an optimal metasurface design would be based on a set of meta-atoms that offer a complete phase modulation (from 0 to 2π) and simultaneously a high reflection or transmission efficiency. An intuitive plasmonic meta-atom design would be based on a single rod antenna, which exhibits a strong light–matter interaction through its electric dipole resonances.^[45] However, a single rod antenna features in principle at most π phase change governed by the first-order electric dipole resonance, while accompanied with a strong amplitude variation (Figure 2A). An empirical formula is used to predict the dipolar resonance of a perfect electric conductor, suggesting the resonance wavelength to be roughly twice of the length of the rod antenna.^[21] However, this empirical formula prediction becomes worse for metallic structures at high frequencies

(e.g., optical frequencies), particularly when approaching the plasmon resonance of metals.^[46,47] For instance, our simulated silver nanorod with a length of 320 nm on glass (414 nm for a freestanding silver nanorod in the air) forms an electric resonance at a wavelength of 1.57 μ m (inset of Figure 2A).

To achieve complete phase modulation in plasmonic metasurfaces, magnetic resonance has been exploited,^[48,49] which can be supported by a metal–insulator–metal (MIM) structure that consists of a metallic subwavelength structure and a continuous metal film separated by a thin dielectric spacer. The MIM structure supports a magnetic resonance mode, which is also known as gap surface plasmon resonance.^[49] When the MIM structure is illuminated by a linearly polarized field along the long axis of the metallic structure, antiparallel electric currents can be induced on two metallic layers due to the coupling between them, leading to an effective magnetic mode with a strongly enhanced magnetic field in the spacer dielectric layer. The MIM structure under the magnetic resonance allows the complete phase modulation covering the full 2π range, as well as a high reflection amplitude due to the total reflection by the metallic ground plane (Figure 2B). As an example, the induced antiparallel electric currents in the simulated silver nanostructure and the silver ground plate represent the excitation of the magnetic resonance at 1.44 μ m (inset of Figure 2B). As such, plasmonic metasurfaces in a MIM configuration have been used for high-efficiency phase modulation in copolarization response (the same polarization as the incident light).^[22]

In addition to the copolarization response, cross-polarized radiation (orthogonal polarization with respect to the incident light) offers another path for the phase modulation, the response of which depends on the design of a subwavelength wave plate that can be mathematically formulated by the Jones matrix calculus.^[50] To offer strong cross-polarization conversion, the subwavelength metallic structure in the top layer of a MIM structure can be designed into a rectangular bar that exhibits strong birefringence (Figure 2C). Its optical response can be predicted based on the Jones matrix: $M = \begin{bmatrix} A_o e^{i\varphi_o} & 0 \\ 0 & A_e e^{i\varphi_e} \end{bmatrix}$,

in which A_o , A_e and φ_o , φ_e represent the amplitude and phase coefficients for the linear polarization along the long and short axes of the subwavelength metallic bar, respectively. Without loss of generality, the meta-atom under the illumination of left-handed circular polarization (LCP) can be mathematically given as: $|\psi\rangle = \Gamma(-\Phi)M\Gamma(\Phi)|L\rangle$, where $\Gamma(\Phi)$ is the rotation matrix at an in-plane angle of Φ . As such, the meta-atom at the rotational angle Φ can be expressed

by: $|\psi\rangle = \frac{e^{i\frac{\varphi_o + \varphi_e}{2}}}{2\sqrt{2}} \begin{bmatrix} A_o e^{i\varphi_o} (1 + e^{-i2\Phi}) + A_e e^{-i\varphi_o} (1 - e^{-i2\Phi}) \\ iA_o e^{i\varphi_o} (1 - e^{-i2\Phi}) + iA_e e^{-i\varphi_o} (1 + e^{-i2\Phi}) \end{bmatrix}$, with $\varphi_\Delta = \frac{\varphi_o - \varphi_e}{2}$.

After passing through the meta-atom, part of the LCP polarization is converted to the right-handed circular polarization (RCP) accompanied with a local geometric phase (-2Φ): $\langle R|\psi\rangle = \frac{1}{2}(A_o e^{i\varphi_o} - A_e e^{i\varphi_e})e^{-i2\Phi}$. The cross-polarization conversion efficiency (CE) can be calculated as: $CE = |\frac{1}{2}(A_o e^{i\varphi_o} - A_e e^{i\varphi_e})|^2$. The dimensions of the rectangular structure can be carefully designed to have a dominant cross-polarization response, exhibiting an in-plane rotation angle-induced geometric phase $- (+)2\Phi$ for the LCP (RCP) illumination (Figure 2C). This

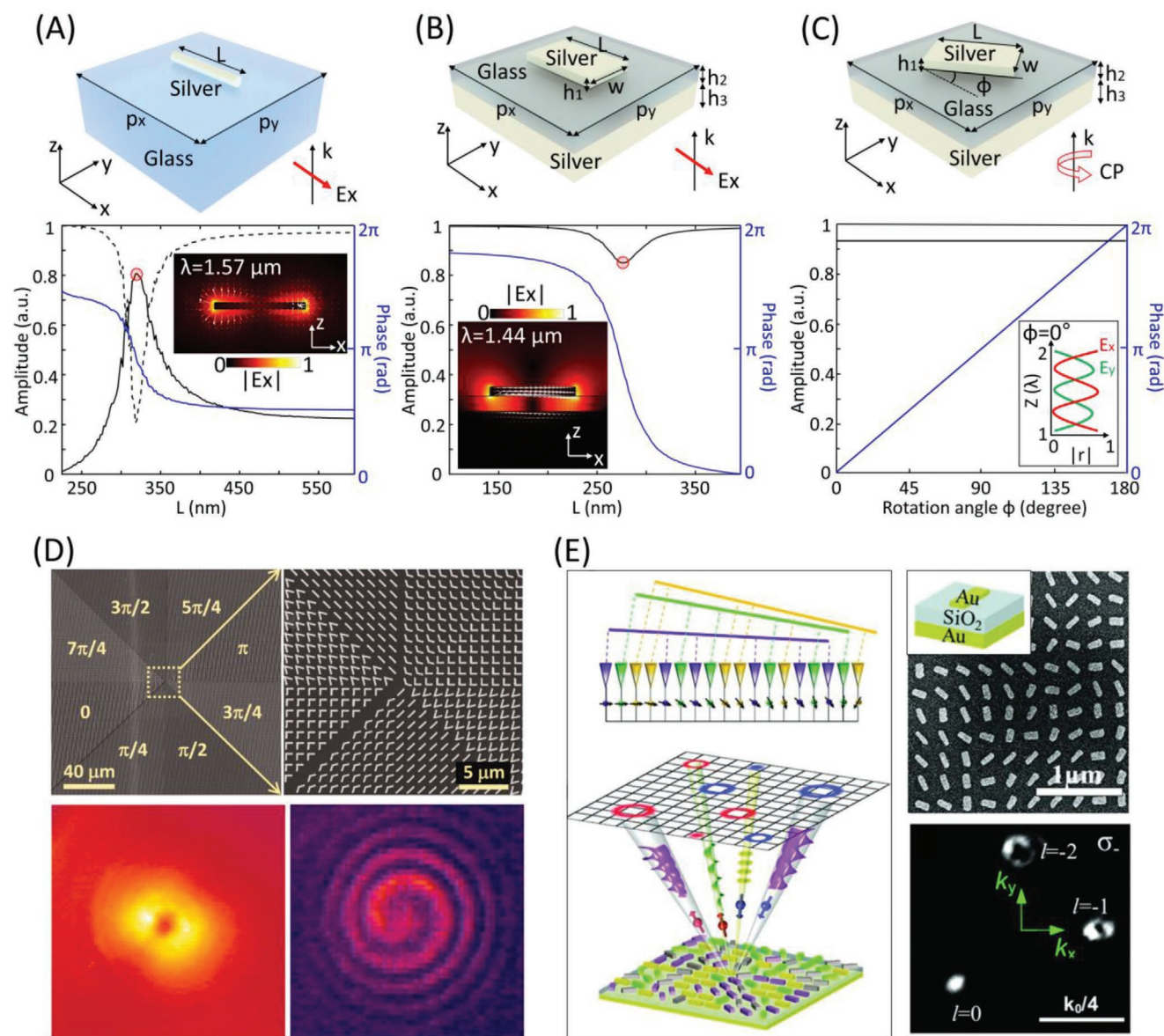


Figure 2. Design principle of metasurfaces in reflection and exemplary plasmonic metasurfaces for OAM generation in real space. A) Metasurface design based on electric resonance in a plasmonic rectangular structure. Inset: electric field distribution in a cross-section plane of a silver rectangular structure with a length of 320 nm under the electric resonance at $\lambda = 1.57 \mu\text{m}$, where the white arrows represent electric field vectors. The simulated meta-atom structure has a width and a height of 30 nm, sitting on a glass substrate with a pitch distance ($p_x = p_y$) of 800 nm. B) A copolarization metasurface design based on magnetic resonance in a MIM configuration. Inset: electric field distribution in a cross-section plane of a MIM meta-atom structure under the magnetic resonance at $\lambda = 1.44 \mu\text{m}$, where the white arrows represent induced current density. The labeled parameters are: $p_x = p_y = 500 \text{ nm}$, $w = 200 \text{ nm}$, $L = 282 \text{ nm}$, $h_1 = 30 \text{ nm}$, $h_2 = 50 \text{ nm}$, $h_3 = 80 \text{ nm}$. C) Cross-polarization geometric metasurface design based on magnetic resonance in a MIM configuration. Inset: transverse electric fields distributions along the propagation direction, suggesting a nearly equal amplitude and a π phase difference between the reflected E_x and E_y fields. The labeled parameters are the same as the ones in (B). D, E) Exemplary real-space metasurface generation of OAM beams in reflection, based on a V-shaped plasmonic metasurface (D)^[21] and a gold MIM metasurface (E).^[22] D) Reproduced with permission.^[21] Copyright 2011, American Association for the Advancement of Science. E) Reproduced with permission.^[22] Copyright 2016, American Association for the Advancement of Science.

geometric phase response is also known as the Pancharatnam–Berry phase in recognition of Pancharatnam and Berry’s independent discoveries of this phenomenon.^[51,52] As such, complete phase modulation ($0-2\pi$) with a high efficiency can be achieved by rotating the metallic bar in the MIM configuration and the metallic bar works as a miniature half wave plate (inset of Figure 2C).

Apart from the geometric metasurface with strong cross-polarization conversion in the circular polarization, strong cross-polarization can also be implemented for linear polarization. Plasmonic hybridization in a V-shaped plasmonic antenna allows the near-field interference of two electric resonances,^[21] increasing the phase tuning range of plasmonic meta-atoms based on orthogonal linear polarizations. Plasmonic

metasurfaces with a high resolution have been designed and fabricated to create vortex beams carrying OAM.^[21] As an example, a plasmonic metasurface consisting of eight V-shape antennas introduces a spiral-like phase shift with respect to the planar wavefront of the incident light, creating a vortex beam with $l = +1$ in real space (Figure 2D). The vortex beam has an annular intensity distribution in the cross-section, the dark region at the center corresponds to a phase singularity. The spiral wavefront of the vortex beam can be revealed by interfering the beam with a copropagating Gaussian beam, producing a spiral interference pattern. As another example of metasurface generation of OAM in real space, a plasmonic metasurface in a MIM configuration was developed to generate multiple spin-dependent optical vortices,^[22] in which the MIM nanoantennas were randomly distributed into equal interleaved subarrays (Figure 2E). The far-field intensity distribution by illuminating the metasurface with circularly polarized light verifies the generation of three spin-dependent OAM wavefronts with $l = 0, -1, \text{ and } -2$.

2.2. Dielectric Metasurfaces

Even though plasmonic metasurfaces can be designed for efficient wavefront manipulation, it works for reflected light from the metasurface. All-dielectric metasurfaces have been developed to achieve highly efficient wavefront shaping for transmitted light. Huygens' metasurfaces,^[53] which spectrally overlap electric and magnetic resonances of equal strength, have been developed to demonstrate full phase coverage in transmission with high efficiency. Here, we consistently used a low-loss amorphous silicon (a-Si) material to simulate various meta-atom designs with different physics. As an example, we show that an a-Si nanodisk with an ultrathin thickness of only 220 nm can be designed to satisfy the Kerker condition for a Huygens' metasurface, wherein electric dipole resonance (EDR) and magnetic dipole resonance (MDR) are spectrally overlapped to cover the full phase coverage (inset of Figure 3A).

In addition to Huygens' metasurfaces, a high-index dielectric nanopillar can be designed as a truncated waveguide with modal dispersion,^[54,55] and each spatial mode has a different effective mode index for light transmission. For a nanopillar with a symmetric transverse cross-section, its phase response depends on the spatial modes supported by the waveguide: $\varphi(n_{\text{eff}}, H) = kn_{\text{eff}}H$, where n_{eff} and H represent the effective mode index and height of the nanopillar, respectively. Since a typical metasurface has a uniform height (e.g., metasurfaces fabricated via an etching process), its phase response solely depends on the effective mode index: $\varphi(n_{\text{eff}}) = kn_{\text{eff}}H$. As such, to achieve full 2π phase modulation, the effective mode index tuning range should satisfy at least: $\Delta(n_{\text{eff}}) = \lambda/H$, where λ is the wavelength of incident light. We simulated an a-Si nanopillar with a constant height of 1 μm to support the full phase modulation and simultaneously high transmission efficiency (Figure 2B). Higher order waveguide-like cavity resonances inside the a-Si nanopillar can be evidenced from the optical fields concentrated inside the dielectric nanopillars (inset of Figure 2B), although some electric fields on the corners of the

nanopillar might present some scattering loss and near-field interactions with neighbor structures.

A high-index asymmetric nanopillar waveguide can be designed as a subwavelength wave plate with strong birefringence, exhibiting different phase responses for the polarization along the long and short axes.^[56,57] This asymmetric nanopillar supports two classes of waveguide modes: transverse modes $n_{1_{\text{eff}}}$ along the long axis and $n_{s_{\text{eff}}}$ along the short axis, respectively. Like the symmetric nanopillar waveguide, the phase response of an asymmetric nanopillar waveguide can be calculated as: $\varphi_l(n_{1_{\text{eff}}}, H) = kn_{1_{\text{eff}}}H$ and $\varphi_s(n_{s_{\text{eff}}}, H) = kn_{s_{\text{eff}}}H$ for the polarization along the long and short axes, respectively, where k is the wavevector of incident light. This anisotropic phase accumulation allows the design of an all-dielectric geometric metasurface with both high transmission and polarization conversion efficiencies. A local geometric phase response of $- (+)2\Phi$ can be acquired by rotating the asymmetric nanopillar with an orientation of Φ for the LCP (RCP) illumination. As an example, we show that the in-plane rotation angle Φ of a rectangular a-Si nanopillar meta-atom can control the full phase modulation (Figure 3C). To visualize the strong birefringence property of the simulated a-Si nanopillar, we placed the a-Si nanopillar to be 45° in the in-plane rotation angle and illuminate it with polarized light along the x -axis (E_x). After passing through the nanopillar, most of the electric field amplitude is converted from E_x to E_y , representing the function of a half wave plate (inset of Figure 3C).

Thus far, our discussion focuses on geometric metasurfaces composed of identical meta-atoms with spatially varying orientation (ϕ), which perform the general spin-to-orbital angular momentum conversion of $|L\rangle \rightarrow |R\rangle e^{-2\varphi}$ and $|R\rangle \rightarrow |L\rangle e^{2\varphi}$,^[58] where $|L\rangle$ and $|R\rangle$ represent the LCP and RCP polarizations, respectively. Because of the constant meta-atom design, the output phase response for the LCP and RCP illuminations, including the generated OAM states, are not independent and they are constrained to be conjugate values. Moreover, geometric metasurfaces are typically limited to the interaction with orthogonal circular polarizations that represent only two of an infinite set of possible polarizations on the Poincaré sphere. Recently, multidimensional metasurfaces consisting of meta-atoms with both varying orientations and sizes have been developed to control arbitrary orthogonal polarizations.^[59,60] More importantly, the output phase response for arbitrary orthogonal polarizations can be decoupled from each other, leading to a new concept of arbitrary spin-to-orbital angular momentum conversion of light.^[23] Such multidimensional metasurfaces can be designed by exploiting the complete and independent phase and polarization control of a single meta-atom based on the Jones matrix calculus.^[24] In this case, a multidimensional metasurface can perform two independent transformations: i) $|\lambda^+\rangle \rightarrow e^{i\varphi} |(\lambda^+)^*\rangle$; ii) $|\lambda^-\rangle \rightarrow e^{i\varphi} |(\lambda^-)^*\rangle$, where $|\lambda^+\rangle$ and $|\lambda^-\rangle$ denote arbitrary orthogonal states on the Poincaré sphere, the output polarizations $|(\lambda^+)^*\rangle$ and $|(\lambda^-)^*\rangle$ have opposite handedness with respect to their original polarizations. As such, a dielectric metasurface that performs the specific mappings of $|L\rangle \rightarrow |R\rangle + 3\rangle$ and $|R\rangle \rightarrow |L\rangle + 4\rangle$ has been realized for the metasurface generation of OAM modes in real space (Figure 3D–F).^[23] Recently, a similar metasurface design by exploiting the independent and complete phase modulation on

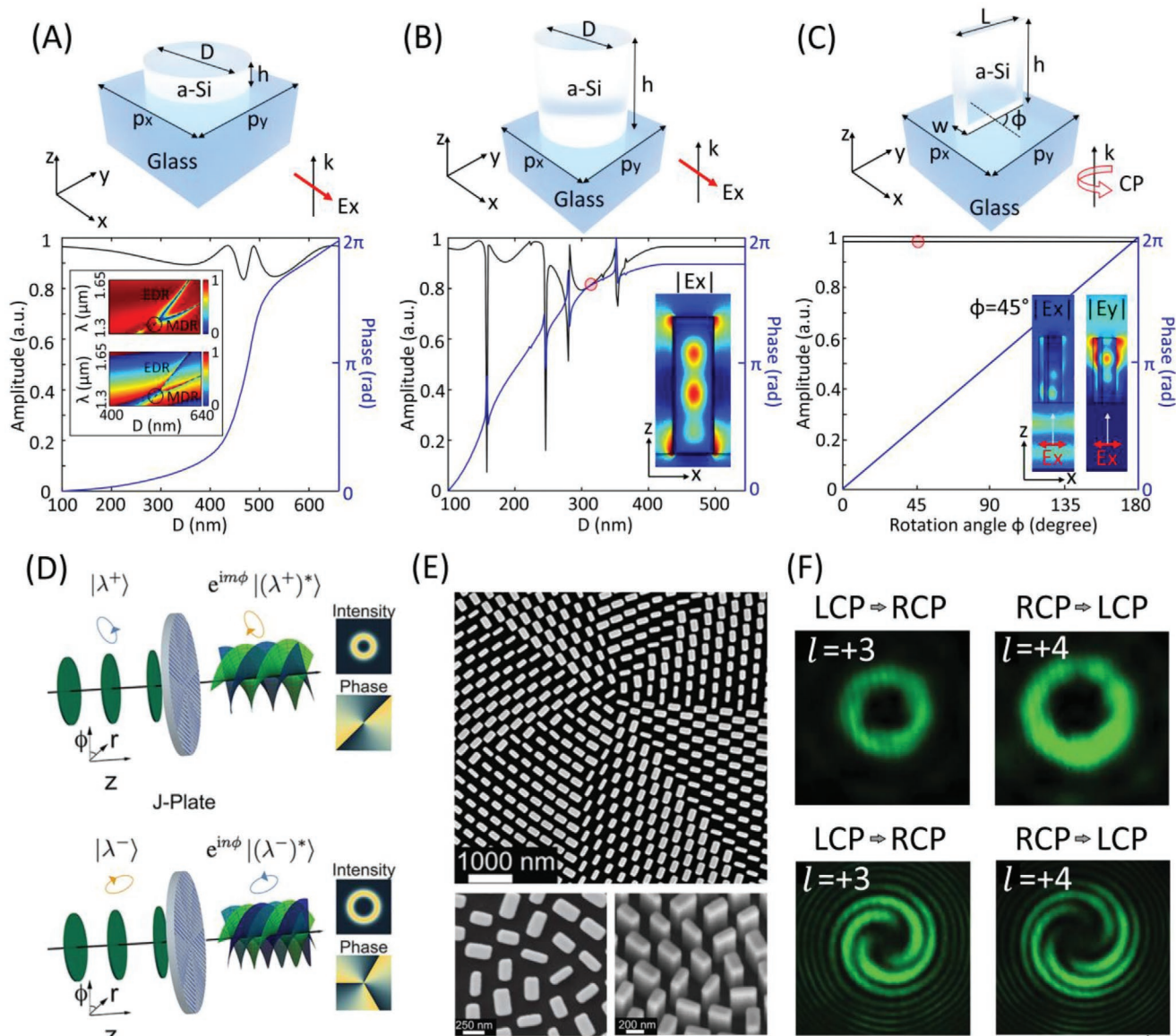


Figure 3. Design principle of metasurfaces in transmission and exemplary dielectric metasurfaces for the OAM generation in real space. A) Huygens' metasurface design based on the interference of multiple Mie resonances. Inset: the Kerker condition achieved from spectrally overlapping electric dipole resonance (EDR) and magnetic dipole resonance (MDR) at $\lambda = 1336$ nm. Labeled parameters: h : 220 nm, $p_x = p_y = 660$ nm. B) Copolarization metasurface design based on a truncated dielectric waveguide. Inset: electric field distribution in a cross-section plane of the meta-atom, showing a strong cavity mode inside the waveguide at $\lambda = 1.4$ μ m. Labeled parameters: h : 1 μ m, $p_x = p_y = 600$ nm. C) Cross-polarization metasurface design based on a birefringent dielectric waveguide. Inset: electric field distribution in a cross-section plane of the meta-atom with a rotation angle $\Phi = 45^\circ$, exhibiting strong polarization conversion from incident E_x field to E_y field at $\lambda = 1.4$ μ m. Labeled parameters: h : 1 μ m, $w = 225$ nm, $L = 450$ nm, $p_x = p_y = 600$ nm. D–F) Exemplary real-space metasurface generation of OAM beams in transmission based on arbitrary spin-to-orbital angular momentum conversion (D), based on a hybrid dielectric metasurface with both dynamic and geometric phase manipulations (E). The experimental results of spin-decoupled OAM fields are given in (F). D–F) Reproduced with permission.^[23] Copyright 2017, American Association for the Advancement of Science.

orthogonal linear polarization states has been realized for the simultaneous generation of high purity OAM states of $l = +10$ and $+100$ for the x - and y -linearly polarized incident light, respectively.^[61] In addition, a dielectric metasurface, capable of switching between a Gaussian phase profile and an OAM spiral phase profile through incident circular polarization states, has been realized for bright-field and isotropic edge-enhanced phase contrast imaging, respectively.^[62]

3. Metasurface Generation of OAM in Momentum Space

3.1. OAM-Preserving Metasurfaces

Metasurface technology has transformed the field of optical holography by developing ultrathin metasurface holograms that use subwavelength meta-atom pixels for unprecedented control

of the amplitude, phase, and polarization of light. However, the bandwidth of a metasurface hologram has remained too low for practical use, even though polarization,^[60,63,64] wavelength,^[65,66] and incident angles of light^[67] have been exploited for metasurface holographic multiplexing.

Twisted light with an unbounded set of orthogonal OAM modes holds great promise to increase the bandwidth of a metasurface hologram. To achieve the OAM sensitivity, a hologram needs to be designed in momentum (Fourier) space.^[25–27,68] To preserve the OAM property in each pixel of a reconstructed holographic image (the momentum space of a Fourier hologram), it is necessary to spatially sample the holographic image by an OAM-dependent 2D Dirac comb function to avoid spatial overlap of the helical wavefront kernel, creating OAM-pixelated images (Figure 4A). The constituent spatial frequencies of an OAM-preserving metasurface hologram (OPMH) add a linear spatial frequency shift together with a helical wavefront to an incident plane-wave beam (k_{in}). As such, outgoing spatial frequencies leaving the OPMH (k_{out}) possess an individually controlled helical wavefront, which implies that the OPMH could create OAM-pixelated holographic images in the momentum space. An OPMH consisting of subwavelength gallium nitride (GaN) nanopillars with a fixed height of 1 μm and various radii was recently realized based on the phase-only modulation (Figure 4B).^[25] OPMHs allow lensless reconstruction of OAM-carrying holographic images with topological charges of $l = \pm 1$ and ± 2 with image sampling (to preserve the OAM property) constants of 19.8 and 26.1 μm , respectively. Notably, adding a spiral phase profile onto each spatial frequency component of an OAM-preserved hologram allows the design of an OAM-selective hologram,^[25] through which different incident OAM modes can be simultaneously detected in the momentum space.^[69]

Even though the phase-only metasurface hologram was first developed for OAM holography,^[25] the neglected amplitude information breaks the linear superposition principle for holographic multiplexing and incurs strong crosstalk.^[27] Mathematically, a complex-amplitude hologram with independent amplitude and phase control could allow the superposition principle to continue to hold and hence eliminating holographic multiplexing crosstalk. Recently, a complex-amplitude metasurface hologram was developed to achieve ultrahigh-dimensional OAM-multiplexing holography in momentum space.^[27] Unlike the typical metasurface with restricted degrees of freedom in a 2D plane, a novel metasurface fabrication platform based on 3D laser nanoprinting unlocks the height degree of freedom of a metasurface. Strikingly, the height (h) and in-plane rotation (\mathcal{D}) of a birefringent polymer nanopillar are employed to independently control the amplitude and phase responses of transmitted light, respectively (Figure 4C).

Specifically, a polymer rectangular nanopillar with a low refractive index ($n = 1.52$) and an aspect ratio of up to 15 was used as a 3D meta-atom. Such a high-aspect-ratio nanopillar can be designed to exhibit strong birefringence manifested by converting the polarization states of transmitted light (inset of Figure 4C). 3D laser nanoprinting technology based on two-photon polymerization induced by a femtosecond laser was used to fabricate 3D metasurfaces. Notably, the designed and fabricated 3D meta-atoms can access arbitrary points in the complex plane, leading to a 64-level complex-amplitude metasurface that consists of polymer nanopillars with 8 different

heights having 8 different in-plane rotation angles (Figure 4D). As such, a large-scale complex-amplitude OAM-multiplexing hologram (2.5 mm by 2.5 mm) consisting of 2000 by 2000 pixels was designed and 3D laser nanoprinted (Figure 4E). The inset of Figure 4E shows an optical image of the fabricated metasurface, while the top- and oblique-view scanning electron microscopy images of enlarged areas in the metasurface are presented in the right panel of Figure 4E. As a result, two holographic videos consisting of 60 image frames were experimentally reconstructed from a single metasurface hologram at two different planes in the momentum space (Figure 4F).

3.2. Polarization Optical Vortices in Momentum Space

In addition to the phase vortex control in momentum space, photonic crystal (PhC) slabs possess an inherent polarization vortex in momentum space around bound states in the continuum (BIC) of the periodic structures.^[28–30,70–74] These polarization vortices feature the in-plane winding of a vector field in momentum space, resulting from the topological property of the PhC slabs (Figure 5A). In such a system, the rotational symmetry (higher than twofold) of any singlet at the center of the Brillouin zone (the Γ point) mismatches the symmetry of any plane wave with in-plane wave vector $k_{\parallel} = 0$ (twofold).^[30] As such, this singlet cannot couple to free space, forming a symmetry-protected BIC with an infinite radiative quality factor lying in the continuum. For the resonances near the Γ -point BIC, the resonant guided modes have high radiative quality factors, so that they can couple to the far field. The states of polarization of far-field radiation from these guided resonances are spatially rotating in a closed loop in momentum space, imparting an even-order phase vortex to an optical beam governed by the Pancharatnam–Berry phase (Figure 5B).^[30] As an example, Figure 5C presents the polarization distributions of the isofrequency contours (dashed loops) near the Γ -point BIC of a PhC slab, in which the polarization distributions are labeled as orange arrows. These winding polarization vectors near the Γ -point BIC form a polarization vortex in the momentum space with topological charge of $l = +1$ (Figure 5D), giving rise to a geometric phase response for the LCP and RCP incidences as $|L\rangle \rightarrow |R\rangle e^{-2i\phi}$ and $|R\rangle \rightarrow |L\rangle e^{2i\phi}$, respectively, where ϕ is the azimuthal angle in the transverse plane. Such polarization-induced optical vortices in momentum space have been experimentally observed from the far-field profiles of cross-polarized beams in the Fourier plane of a fabricated PhC slab (Figure 5E). Recently, an ultrathin perovskite film (220 nm thick lead bromide perovskite) perforated with a circular array was developed to realize a BIC-protected polarization vortex laser (Figure 5F).^[72] This ultrathin polarization vortex laser provides a viable approach to achieving ultrafast all-optical switching between the vortex beam lasing and linearly polarized beam lasing (Figure 5G) within only 1–1.5 ps at room temperature.

4. OAM Generation Based on Microcavities

Apart from metasurfaces, dielectric and plasmonic resonators and microcavities with strong mode coupling have recently

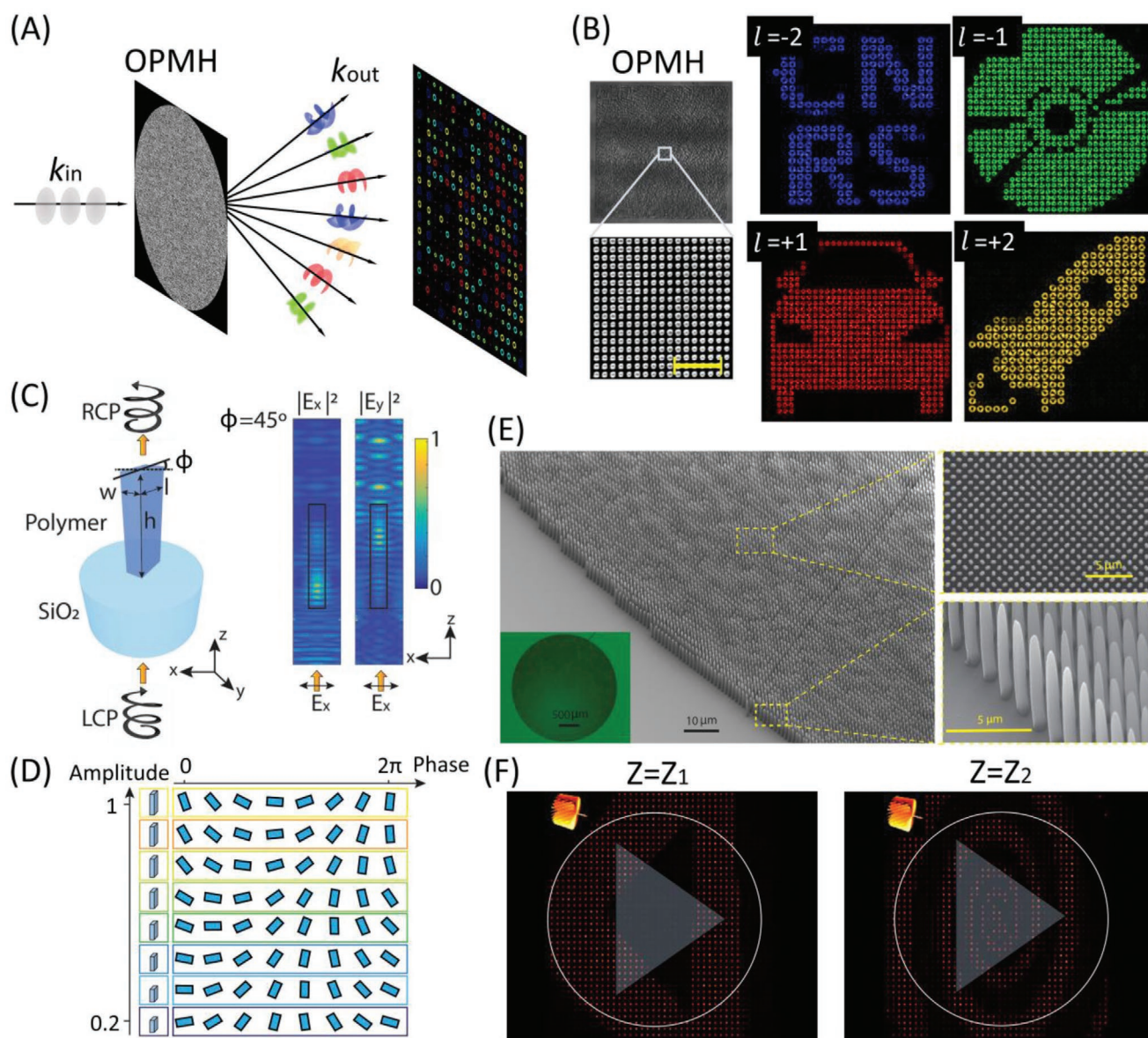


Figure 4. Metasurface generation of phase vortices carrying different OAM modes in momentum space. A) Design of an OAM-preserving metasurface hologram (OPMH) in the momentum space through spatial frequency sampling of the OPMH, capable of parallel generation of different OAM modes in momentum space (Fourier domain of the OPMH). B) Exemplary use of an OPMH made of GaN nanopillar waveguides for the generation of OAM-carrying holographic images in the Fourier plane. C) Schematic of a polymer-based rectangular nanopillar featuring strong birefringence that converts the incident polarization along the x -axis to the one along the y -axis when the nanopillar has a rotation angle of 45° ($\phi = 45^\circ$). w , l , h , and Φ denote the width, length, height, and in-plane rotation angle of a polymer nanopillar, respectively. D) Schematic illustration of 64-level complex-amplitude modulation in the complex plane, based on the selected nanopillars with 8 different heights having 8 different in-plane rotation angles. E, F) Exemplary use of an OPMH made of polymer nanopillars (E) for reconstructing a range of OAM-dependent images in momentum space (F). B) Reproduced under the terms of the CC-BY Creative Commons Attribution 4.0 International licenses (<https://creativecommons.org/licenses/by/4.0/>).^[25] Copyright 2019, The Authors, published by Springer Nature. C–F) Reproduced with permission.^[27] Copyright 2020, The Authors, published by Springer Nature.

been developed for on-chip generation and tuning of different OAM modes.^[31–35,75,76] The first example of vortex microemitters is based on a silicon-integrated microcavity, which uses angular gratings to extract OAM modes confined in degenerate whispering gallery modes (WGM) into free-space beams with well-controlled topological charges (Figure 6A). This WGM microcavity has a small ring diameter of 3.9 μm , embedded with subwavelength angular grating structures along the azimuthal

direction to couple the confined high-quality factor resonant OAM mode into free space. Owing to their high-quality factors, WGM microcavities have recently been developed for achieving vortex microlasers.^[31] By exploiting non-Hermitian photonics at an exceptional point, a vortex microlaser capable of producing a radially polarized vortex lasing mode was demonstrated (Figure 6B).^[32] This WGM-based vortex microlaser has a periodic alternation of single-layer Ge and bilayer Cr/Ge structures

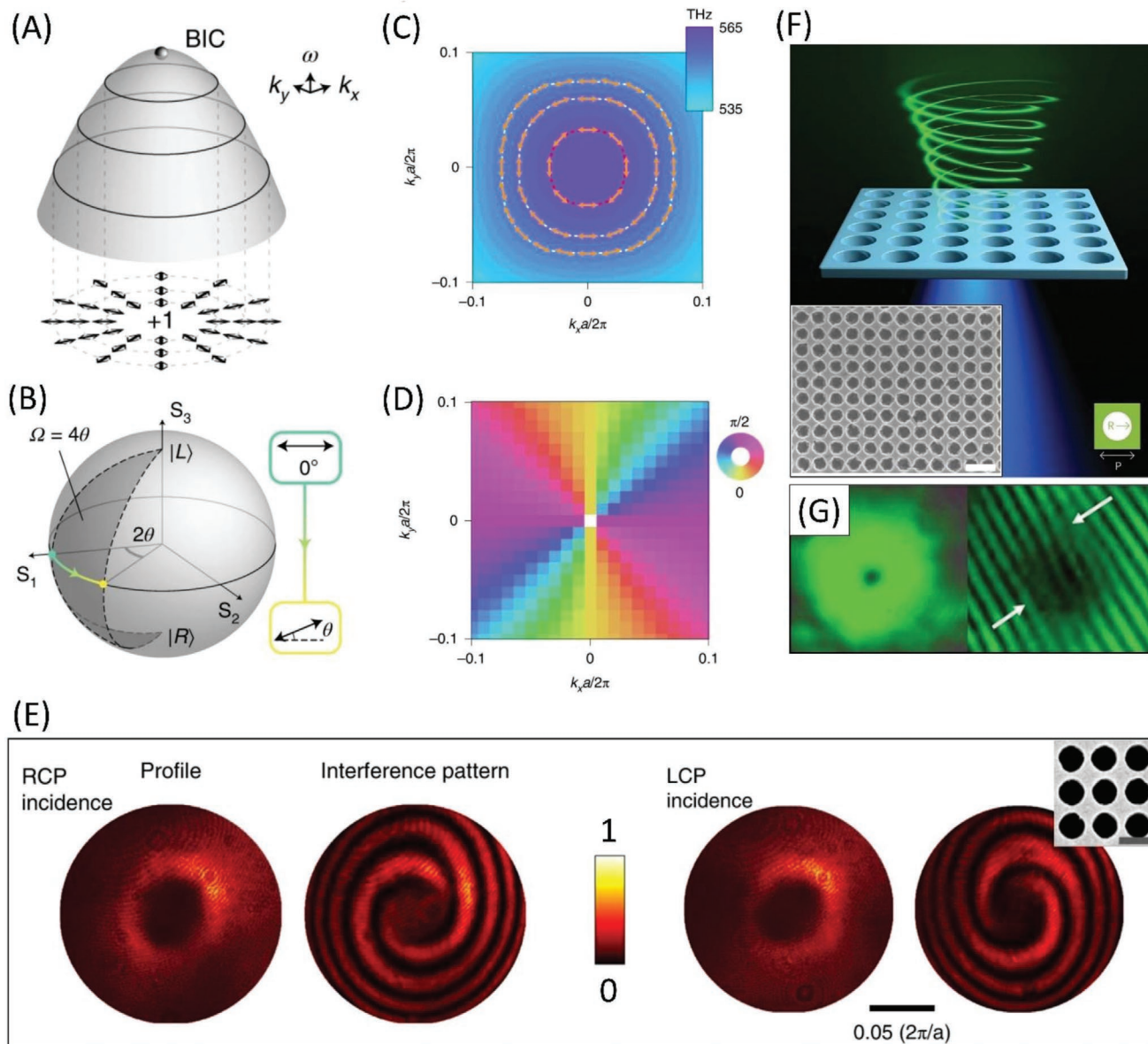


Figure 5. PhC metasurface generation of polarization-induced vortices in momentum space. A) Schematic of a parabolic band of a PhC slab, which has a BIC in the center. The vortex structures formed by nearly linear-polarized guided resonances at different frequencies close to the BIC frequency are projected onto the momentum-space plane. B) Illustration of the vortex generation based on the geometric phase induced by the polarization change on the equator of the Poincaré sphere. C, D) Isofrequency contours (dashed loops) with polarization distributions (orange double-headed arrows) (C) and the azimuthal angle map of polarizations (D). E) Exemplary generation of polarization-induced vortices in momentum space of a PhC metasurface. Inset: the scanning electron microscopy image of the sample with a scale bar of 400 nm. F) Exemplary generation of a green vortex lasing mode in momentum space through pumping a perovskite metasurface by a blue laser. Inset: scanning electron microscopy image of the fabricated perovskite metasurface with a scale bar of 500 nm. G) Measured far-field pattern and the corresponding self-interference pattern of the vortex lasing mode. A–E) Adapted with permission.^[30] Copyright 2020, The Authors, published by Springer Nature. F, G) Adapted with permission.^[72] Copyright 2020, The Authors, published by American Association for the Advancement of Science.

on top of a 500 nm thick InGaAsP multiple quantum wells on an InP substrate.

In addition to passive OAM microcavities, tunable vortex microlasers have also been demonstrated, wherein the helicity of the OAM wavefront can be optically controlled via incident SAM carried by the circular polarization (Figure 6C).^[33] This is based on optically breaking time-reversal rotational

symmetry by spin-polarizing a gain medium with a circularly polarized optical pump, creating spin-dependent vortex emission. This spin-controlled vortex microlaser embeds a single In_{0.05}Ga_{0.95}As quantum well, and spin-orbit coupling arises from the fact that photon hopping in planar microcavities with rotational symmetry is spin-dependent. However, the magnitude of the OAM ($|l|$) is not tunable in a fabricated device, and

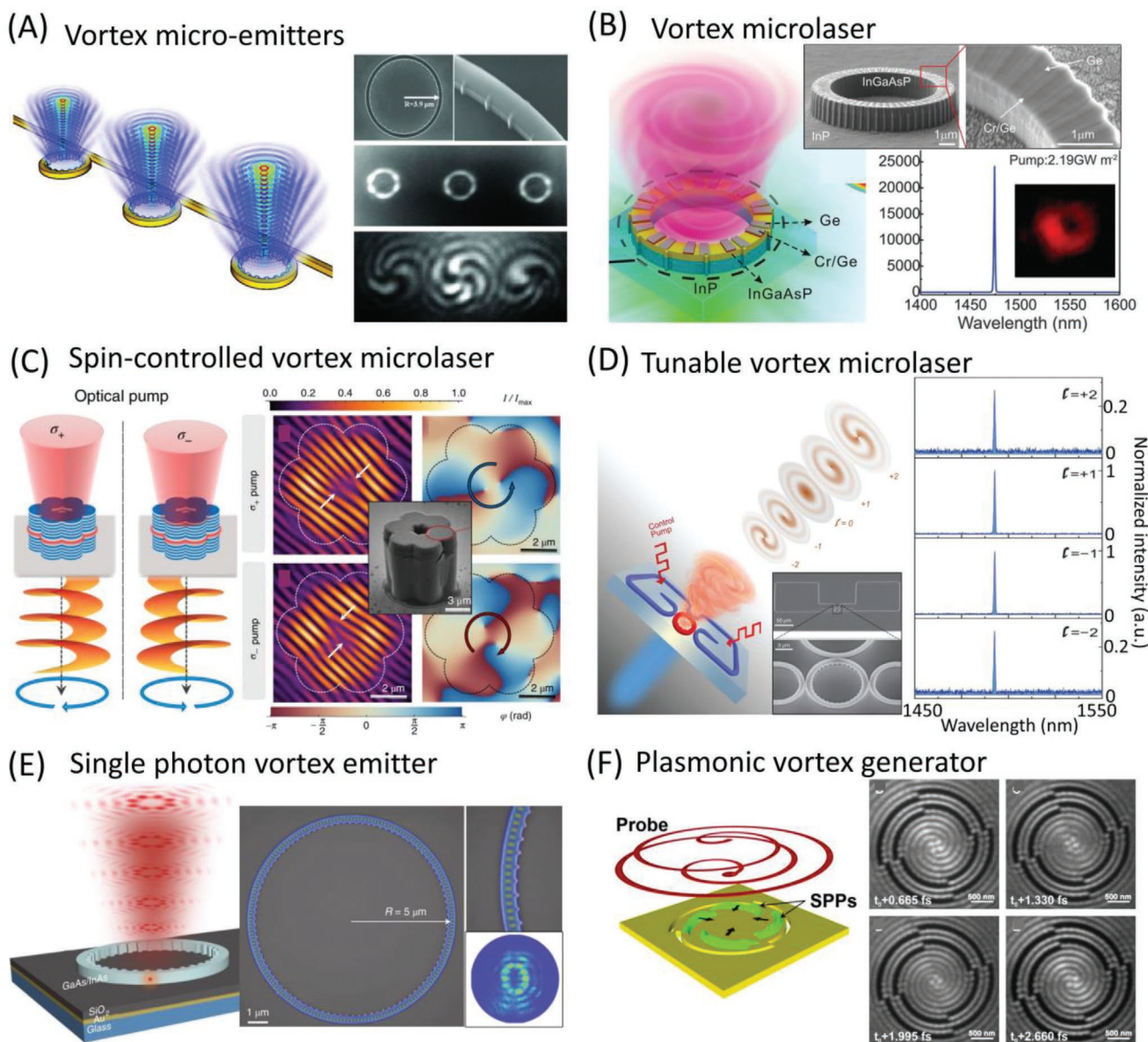


Figure 6. OAM emission and lasing based on microcavities. A) Vortex microemitters based on WGM microcavities engraved with angular gratings. B) A vortex microlaser based on the non-Hermitian photonics design at an exceptional point. C) A spin-controlled vortex microlaser based on the optical breaking of time-reversal symmetry in a semiconductor microcavity. D) A tunable vortex microlaser designed based on the properties of total momentum conservation, spin-orbit interaction, and optical non-Hermitian symmetry breaking. E) A single photon vortex emitter based on the deterministic coupling of single quantum dots to microcavities engraved with angular gratings. F) A plasmonic vortex generator based on sectional Archimedean spiral grooves. A) Reproduced with permission.^[31] Copyright 2012, American Association for the Advancement of Science. B) Reproduced with permission.^[32] Copyright 2016, American Association for the Advancement of Science. C) Reproduced with permission.^[33] Copyright 2019, The Authors, published by Springer Nature. D) Reproduced with permission.^[34] Copyright 2020, The Authors, published by American Association for the Advancement of Science. E) Reproduced with permission.^[35] Copyright 2012, The Authors, published by Springer Nature. F) Reproduced with permission.^[37] Copyright 2017, American Association for the Advancement of Science.

this device also demands a cryogenic environment. Recently, an OAM-tunable vortex microlaser based on photonic spin-orbit interaction and optical non-Hermitian symmetry breaking has been demonstrated,^[34] which allows on-chip generation of tunable OAM states from $l = -2$ to $+2$ at a single telecommunication wavelength at room temperature (Figure 6D). This is controlled by an externally applied non-Hermitian coupling between the cavity modes. However, due to the conservation of

the total angular momentum, this spin-orbit interaction-based OAM generation is inherently limited to a maximal topological charge of $|l| = 2$.

Conventional single photon sources carrying OAM have been realized via the spontaneous parametric downconversion process in bulk nonlinear crystals, with additional bulky spatial light modulator or spiral phase plates to impart OAM beams.^[77] This suffers from a limited range of OAM modes with high

brightness, OAM purity, complexity, and bulkiness of single photon systems. Recently, a bright solid-state single-photon OAM source was realized by the deterministic coupling of single quantum dots to on-chip microcavities with angular gratings (Figure 6E).^[35] This opens the door to fabricate compact single-photon OAM sources on a semiconductor chip. The generation of single photons in an OAM superposition state with a single-photon purity of $g^{(2)}(0)=0.115(1)$ and a collection efficiency of 23(4)% was reported. On the other hand, plasmonics opens the possibility of producing subwavelength OAM modes in a plasmonic vortex field in the near-field region.^[36,37] For example, Figure 6F presents a plasmonic vortex generator that consists of sectional Archimedean spiral grooves in a gold film, which has recently been used to observe the ultrafast dynamics of plasmonic vortices.^[37] Through precisely controlling the number of grooves, as well as the distance between inner and outer radii of each groove, plasmonic vortices carrying different OAM modes can be created. Both long- and short-range plasmonic vortices confined to deep subwavelength dimensions on the scale of 100 nm have been experimentally characterized with nanometer spatial resolution and sub-femtosecond time-step resolution.^[37]

5. OAM Detection in Nanophotonics

In conventional optics, sorting and detecting OAM modes are usually achieved from an interferometer in real space,^[21,22] spatial filtering in momentum space,^[25–27,78] log-polar,^[15–17] spiral polar,^[18] and Laguerre–Gaussian^[19] mode transformations. However, these far-field approaches typically require a large propagation distance to produce OAM-distinct diffraction patterns, restricting the OAM detection to diffraction-limited optical systems that hinder OAM applications for integrated photonics. Plasmonics breaks the diffraction limit by allowing subwavelength localization of light, bridging the size mismatch between high-capacity photonics and nanoscale electronics.^[45,79,80] Nano-plasmonic detection^[38–43,81–84] of OAM modes have recently been achieved through plasmonic structures designed to couple incident OAM beams into distinctive plasmonic fields. For example, a plasmonic OAM photodiode has been designed to detect a single OAM mode based on the principle of near-field holography, through the interference of focused surface plasmon polaritons and an incident optical vortex field.^[38] An incident OAM beam with a given topological charge can be converted into a focused plasmonic field, under which a subwavelength grating array was engraved to transmit the focused plasmonic field into a photodetector (Figure 7A). On-chip OAM multiplexing of broadband light has been realized from a plasmonic chip that consists of OAM mode-sorting nanoring apertures and semicircular nanogrooves in a gold thin film (Figure 7B).^[40] The nanogrooves were designed to convert the incident OAM beams into spatially distinct plasmonic fields at the position of the mode-sorting nanoring apertures. Four OAM-carrying beams were coupled into spatially separate plasmonic vortices that can be selectively transmitted through the mode-sorting nanoaperture waveguides to the far-field. Furthermore, the nonresonant OAM mode-sorting sensitivity by the nanoring apertures enables on-chip OAM multiplexing over a broad bandwidth.

Traditional noble metals such as gold and silver suffer from high metal losses due to interband transitions in the ultraviolet and visible frequency ranges. Topological insulators represent a new class of plasmonic materials with topologically protected electronic surface states and a high refractive index bulk state, making them attractive for various applications in plasmonics^[41,85,86] and condensed matter physics.^[41,87] Recently, complementary metal–oxide–semiconductor (CMOS)-integratable OAM nanometrology in an ultrathin topological insulator film was demonstrated (Figure 7C).^[41] Applying the superior plasmonic response in an ultrathin Sb₂Te₃ film to the linear displacement engineering of plasmonic OAM modes on a nanoscale, a CMOS-integratable OAM nanometrology device with a low modal crosstalk of less than –20 dB was demonstrated. Spatially resolving these plasmonic fields with subwavelength separation distances demands a high numerical aperture microscope by collecting the light scattering from subwavelength nanoapertures. Alternatively, near-field scanning optical microscopy has been used to directly image the OAM-based linear displacement of plasmonic fields with nearly 120 nm spaced mode intervals (Figure 7D).^[39]

Nevertheless, strong dissipation of the highly localized OAM-distinct plasmonic fields in the near-field region hinders on-chip OAM transmission and processing. Superior transmission efficiency is offered by semiconductor nanowires sustaining highly confined optical modes, but only the polarization degree of freedom has been utilized for their selective excitation.^[88,89] Until recently, an OAM-controlled hybrid nanowire plasmonic circuit was introduced.^[43] Incident OAM beams with different topological charges offer a selective response on the excitation of single-crystalline cadmium sulfide nanowires, through coupling OAM-distinct plasmonic fields into nanowire waveguides for long-distance transportation on-a-chip. For instance, two nanowires transferred on a gold film with a splitting angle of 30° have been used to selectively couple the plasmonic fields excited from incident OAM beams of $l = -4$ and $+4$ for low-loss transportation (Figure 7E). An OAM-controlled optical logic operations including AND and OR gates were experimentally demonstrated through transferring the OAM signals into photoluminescence signals from nanowires.^[43]

To design an OAM-multiplexing chip, it is always important to consider both the number of multiplexing channels and multiplexing crosstalk. Recently, on-chip spin-Hall nanogratings were developed for simultaneously detecting phase and polarization helicities (Figure 7F).^[42] This nanograting is symmetry-breaking with different periods for the upper and lower parts, which enables the unidirectional excitation of the surface plasmon polariton depending on the topological charge of the incident OAM beam. Additionally, spin-Hall metaslits^[90] are integrated onto the grating so that the structure has a chiral response for polarization detection. However, plasmonic devices mentioned so far rely on coupling OAM photons into spatially distinct surface plasmon polaritons and converting the coupled plasmonic fields into photons again via scattering, the latter of which typically involves strong loss. Alternatively, a novel concept of OAM-dependent photocurrent detection was recently introduced.^[44] This is based on the OAM-dependent photogalvanic effect: the generated photocurrent is proportional to the helical phase gradient. OAM-carrying incident

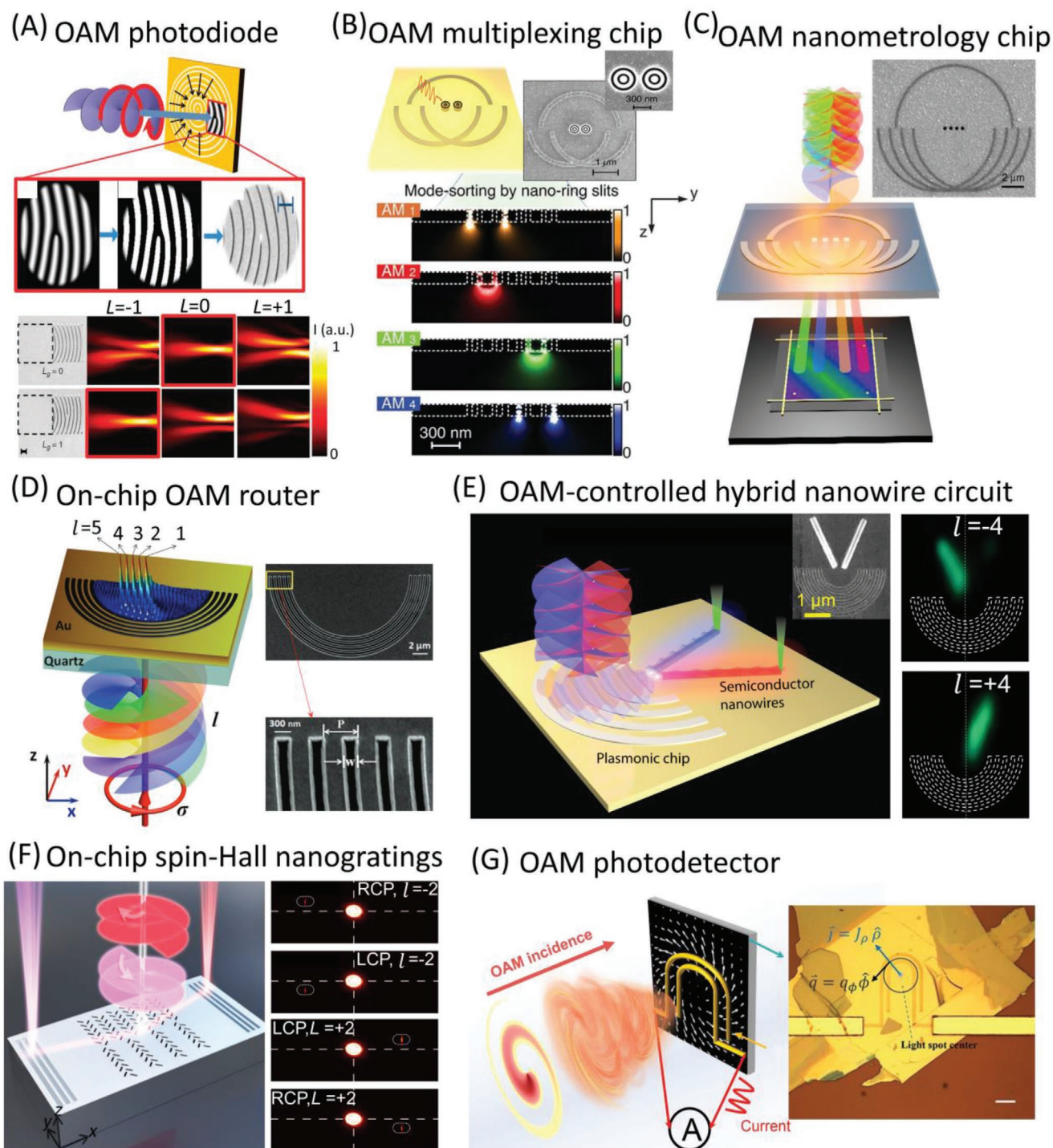


Figure 7. Nanophotonic devices for the OAM detection. A) Design of an OAM photodiode based on the near-field holography principle. B) An OAM-multiplexing chip consisting of plasmonic grooves and mode-sorting nanoring apertures. C) An OAM nanometrology chip based on a plasmonic topological insulator thin film. D) On-chip OAM sorting based on near-field scanning optical microscopy. E) An OAM-controlled hybrid nanowire circuit based on the integration of plasmonic grooves with semiconductor nanowires. F) Design of on-chip spin-Hall nanogratings for on-chip sorting both SAM and OAM with small crosstalk. G) An OAM photodetector based on the OAM photogalvanic effect, in which tungsten ditelluride is integrated with electrodes for direct characterization of topological charge of different OAM modes. A) Reproduced with permission.^[38] Copyright 2012, Springer Nature. B) Reproduced with permission.^[40] Copyright 2016, American Association for the Advancement of Science. C) Reproduced under the terms of the CC-BY Creative Commons Attribution 4.0 International license (<https://creativecommons.org/licenses/by/4.0>).^[41] Copyright 2017, The Authors, published by Springer Nature. D) Reproduced with permission.^[39] Copyright 2015, Royal Society of Chemistry. E) Reproduced with permission.^[43] Copyright 2021, American Chemical Society. F) Reproduced under the terms of the CC-BY Creative Commons Attribution 4.0 International license (<https://creativecommons.org/licenses/by/4.0>).^[42] Copyright 2020, The Authors, published Springer Nature. G) Reproduced with permission.^[44] Copyright 2020, The Authors, published by American Association for the Advancement of Science.

beams are modulated into left- and right-handed circular polarization states, showing distinctive photocurrent responses that are proportional to the OAM topological charge. The electrodes were designed into a U shape on tungsten ditelluride substrate for collecting the photocurrent signals (Figure 7G).

6. Current Challenges and Future Perspective

Thus far, we have provided a detailed review on nanophotonic materials and devices recently developed for the generation and detection of twisted light carrying different OAM modes (Figures 2–7). Even though our highlighted nanophotonic structures and devices only take up a tiny portion of nanophotonic devices developed in the last decade, we anticipate that our review could have covered some of major concepts and hopefully provided a useful guidance on the material and structure choices for twisted light applications. Here, we list and compare some key properties of different metasurface designs that could be used for OAM generation in real space (Table 1). It is clear to see that high efficiency metasurfaces can be designed for both co- and cross-polarization responses in both reflection and transmission. For reflection metasurfaces, plasmonic materials featuring MIM configurations can be applied. For transmission metasurfaces, low-loss and high-index dielectric meta-atoms featuring an ultrathin thickness ($<\lambda$) or a relatively large thickness ($\approx\lambda$) can be designed for Huygens and waveguide-type metasurfaces, respectively. However, for the most accurate phase digitalization when considering the fabrication error, geometric metasurfaces exploiting the rotation-angle-controlled phase response are more desired.

It should be mentioned that metasurface fabrication today involves a costly and time-consuming nanofabrication process. More specifically, planar metasurface fabrication usually relies on the use of electron-beam lithography followed by a reactive-ion dry etching process, ending up with 2D metasurface of uniform height. Even though 3D laser nanoprinting technology offers a cheaper solution to fabricate large-scale 3D metasurfaces with unlocked height degree of freedom, a relatively low spatial resolution (pitch distance $\approx 1\ \mu\text{m}$) and a long processing time hinder its application for mass production of metasurface

devices. Nevertheless, 3D laser nanoprinting technology could be useful for interfacing metasurfaces with fiber-end surfaces for optical fiber functionalization.^[91,92] On the other hand, nanoimprinting lithography may provide a viable approach to producing large-scale, low-cost, and high yield metasurfaces,^[93–95] although it faces two general challenges: overlay alignment and template fabrication. In addition to the fabrication challenges, most metasurface devices are still passive and unlikely to be able to dynamically switch OAM modes. Recent development of spatiotemporal OAM beams^[91,92] and nonlinear OAM conversion,^[98] as well as active metasurfaces^[99,100] promises new hopes to address this key challenge in the future.

Although OAM-preserved metasurfaces could be designed for parallel OAM generation, detection, and processing in momentum space, the number of OAM modes is fundamentally limited by the Nyquist–Shannon sampling theorem and diffraction limit of light.^[27] This makes a trade-off between the number and the highest order of the OAM modes. In addition, extending the OAM selectivity from a 2D Fourier plane to 3D momentum space for 3D holography and other applications remains a challenge. On the other hand, main advantages of the BIC-induced polarization vortices in momentum space include robustness, which can be destroyed only by a large structural variation in the PhC slab, alleviation of coaxial alignment of the incident beam with the structure center, as well as unrestricted choice of materials for a broad frequency range. However, such systems designed near the BIC at the Γ point are typically sensitive to the incident wavelength and incident angle that may easily break the system symmetry.

Apart from metasurfaces developed for twisted light applications, we compare some key properties of different microcavities and plasmonic structures designed for on-chip OAM generation (including OAM lasing) and detection, respectively (Table 2). For the OAM generation, it is expected to see the future development of more efficient, compact, ultrafast, and tunable OAM microcavities that can dynamically switch different OAM modes that are currently limited to a few lower orders. For the OAM detection, developing low-loss materials for on-chip OAM sorting, implementing the OAM sorting structures with optoelectronic components for all-on-chip

Table 1. Comparison of different metasurfaces used for OAM generation. Metasurfaces are divided into four different types: dynamic phase metasurfaces, geometric metasurfaces, hybrid metasurfaces (both dynamic and geometric phase responses are used), and photonic crystal (PhC) slabs.

Type	Material	Meta-atom	Efficiency [%]	Wavelength [μm]	Transmission or reflection	Co- or cross-polarization
Dynamic ^[21]	Gold	V shape	≈ 75	8	Reflection	Cross
Geometric ^[22]	Gold	MIM-rect	≈ 79	0.76	Reflection	Cross
Dynamic ^[53]	Silicon	Ultrathin disk	> 50	1.34	Transmission	Co
Hybrid ^[23]	Titanium dioxide	Rect-nanopillar	NA	0.53	Transmission	Cross
Dynamic ^[25]	Gallium nitride	Circular nanopillar	NA	0.63	Transmission	Co
Hybrid ^[27]	Polymer	Rect-nanopillar	NA	0.63	Transmission	Cross
Hybrid ^[24]	Titanium dioxide	Rect-nanopillar	≈ 52	0.53	Transmission	Cross
PhC ^[30]	Silicon nitride	Hole array	NA	0.53	Transmission	Co
PhC ^[72]	Perovskite	Hole array	NA	0.55	Transmission	Co

Table 2. Comparison of different microcavities and plasmonic structures used for OAM generation and detection, respectively.

Type	Materials	Footprint [μm^2]	Wavelength [μm]	OAM modes
WGM ^[31]	Silicon	16π	1.48–1.58	–4 to +4
WGM ^[32]	InGaAsP	20.25π	1.47	–1
WGM ^[33]	Benzene photonic molecules	10.24π	0.84	–2 to +2 and +3
WGM ^[34]	InGaAsP	12.25π	1.49	–2 to +2
WGM ^[35]	GaAs QDs	25π	0.89–0.92	–8 to +8
Plasmonics ^[38]	Gold	≈ 64	0.63	–1 or +1
Plasmonics ^[40]	Gold	17.64	0.55–0.7	–4 to +4
Plasmonics ^[39]	Gold	222.61	0.63	–5 to +5
Plasmonics ^[41]	Sb ₂ Te ₃ topological insulator	142.04	0.64	–6 to +6
Hybrid ^[43]	Gold–cadmium sulfide nanowires	≈ 63.36	0.49	–4 and +4
Plasmonics ^[84]	Silver	NA	0.63	–3 to +3
Orbital photogalvanic effect ^[44]	Tungsten ditelluride	NA	1	–4 to +4

photocurrent OAM detection, building advanced OAM-controlled hybrid nanocircuits for on-chip OAM information transmission and processing, will make strong impact on future OAM-based photonic chips and communication systems.

In the last decade, nanophotonic materials have been largely exploited for twisted-light manipulation, it is outside the scope of this review to include all the demonstrated concepts in this rapid growing field, readers could also benefit from other review articles.^[1,8,11,68,101–103] Overall, we believe twisted-light manipulation in nanophotonics will continue its exciting journey by making significant impact not only on fundamental understanding of light–matter interactions, but also on wide-ranging applications that benefit from ultracompact, ultrahigh-capacity, and ultrahigh-speed OAM systems-on-a-chip.

Acknowledgements

The authors thank Andreas Aigner for offering helpful comments and suggestions. H.R. acknowledges the funding support from a Macquarie University Research Fellowship (MQRF) from Macquarie University. S.A.M. acknowledges the funding support from the Deutsche Forschungsgemeinschaft, the EPSRC (Grant No. EP/M000044/1), and the Lee-Lucas Chair in Physics.

Open access funding enabled and organized by Projekt DEAL.

Conflict of Interest

The authors declare no conflict of interest.

Keywords

metasurfaces, microcavities, nanophotonics, orbital angular momentum of light, plasmonics

Received: August 25, 2021

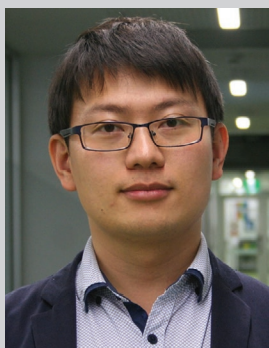
Revised: October 14, 2021

Published online: February 3, 2022

- [1] A. E. Willner, Z. Zhao, C. Liu, R. Zhang, H. Song, K. Pang, K. Manukyan, H. Song, X. Su, G. Xie, Y. Ren, Y. Yan, M. Tur, A. F. Molisch, R. W. Boyd, H. Zhou, N. Hu, A. Minoofar, H. Huang, *APL Photonics* **2021**, 6, 030901.
- [2] J. Wang, J.-Y. Yang, I. M. Fazal, N. Ahmed, Y. Yan, H. Huang, Y. Ren, Y. Yue, S. Dolinar, M. Tur, A. E. Willner, *Nat. Photonics* **2012**, 6, 488.
- [3] Y. Yan, G. Xie, M. P. J. Lavery, H. Huang, N. Ahmed, C. Bao, Y. Ren, Y. Cao, L. Li, Z. Zhao, A. F. Molisch, M. Tur, M. J. Padgett, A. E. Willner, *Nat. Commun.* **2014**, 5, 4876.
- [4] N. Bozinovic, Y. Yue, Y. Ren, M. Tur, P. Kristensen, H. Huang, A. E. Willner, S. Ramachandran, *Science* **2013**, 340, 1545.
- [5] H. Cao, S.-C. Gao, C. Zhang, J. Wang, D.-Y. He, B.-H. Liu, Z.-W. Zhou, Y.-J. Chen, Z.-H. Li, S.-Y. Yu, J. Romero, Y.-F. Huang, C.-F. Li, G.-C. Guo, *Optica* **2020**, 7, 232.
- [6] J. Liu, I. Nape, Q. Wang, A. Vallés, J. Wang, A. Forbes, *Sci. Adv.* **2020**, 6, eaay0837.
- [7] R. Fickler, R. Lapkiewicz, W. N. Plick, M. Krenn, C. Schaeff, S. Ramelow, A. Zeilinger, *Science* **2012**, 338, 640.
- [8] A. Forbes, M. de Oliveira, M. R. Dennis, *Nat. Photonics* **2021**, 15, 253.
- [9] N. Zhao, X. Li, G. Li, J. M. Kahn, *Nat. Photonics* **2015**, 9, 822.
- [10] A. M. Yao, M. J. Padgett, *Adv. Opt. Photonics* **2011**, 3, 161.
- [11] K. Y. Bliokh, F. J. Rodríguez-Fortuño, F. Nori, A. V. Zayats, *Nat. Photonics* **2015**, 9, 796.
- [12] A. T. O’Neil, I. MacVicar, L. Allen, M. J. Padgett, *Phys. Rev. Lett.* **2002**, 88, 053601.
- [13] L. Allen, M. W. Beijersbergen, R. J. C. Spreeuw, J. P. Woerdman, *Phys. Rev. A* **1992**, 45, 8185.
- [14] R. Fickler, G. Campbell, B. Buchler, P. K. Lam, A. Zeilinger, *Proc. Natl. Acad. Sci. USA* **2016**, 113, 13642.
- [15] G. C. G. Berkhout, M. P. J. Lavery, J. Courtial, M. W. Beijersbergen, M. J. Padgett, *Phys. Rev. Lett.* **2010**, 105, 153601.
- [16] M. Mirhosseini, M. Malik, Z. Shi, R. W. Boyd, *Nat. Commun.* **2013**, 4, 2781.
- [17] Y. Guo, S. Zhang, M. Pu, Q. He, J. Jin, M. Xu, Y. Zhang, P. Gao, X. Luo, *Light: Sci. Appl.* **2021**, 10, 63.
- [18] Y. Wen, I. Chremmos, Y. Chen, J. Zhu, Y. Zhang, S. Yu, *Phys. Rev. Lett.* **2018**, 120, 193904.
- [19] N. K. Fontaine, R. Ryf, H. Chen, D. T. Neilson, K. Kim, J. Carpenter, *Nat. Commun.* **2019**, 10, 1865.

- [20] G. Ruffato, M. Girardi, M. Massari, E. Mafakheri, B. Sephton, P. Capaldo, A. Forbes, F. Romanato, *Sci. Rep.* **2018**, *8*, 10248.
- [21] N. Yu, P. Genevet, M. A. Kats, F. Aieta, J.-P. Tetienne, F. Capasso, Z. Gaburro, *Science* **2011**, *334*, 333.
- [22] E. Maguid, I. Yulevich, D. Veksler, V. Kleiner, M. L. Brongersma, E. Hasman, *Science* **2016**, *352*, 1202.
- [23] R. C. Devlin, A. Ambrosio, N. A. Rubin, J. P. B. Mueller, F. Capasso, *Science* **2017**, *358*, 896.
- [24] M. Liu, P. Huo, W. Zhu, C. Zhang, S. Zhang, M. Song, S. Zhang, Q. Zhou, L. Chen, H. J. Lezec, A. Agrawal, Y. Lu, T. Xu, *Nat. Commun.* **2021**, *12*, 2230.
- [25] H. Ren, G. Briere, X. Fang, P. Ni, R. Sawant, S. Héron, S. Chenot, S. Vézian, B. Damilano, V. Brändli, S. A. Maier, P. Genevet, *Nat. Commun.* **2019**, *10*, 2986.
- [26] X. Fang, H. Ren, M. Gu, *Nat. Photonics* **2020**, *14*, 102.
- [27] H. Ren, X. Fang, J. Jang, J. Bürger, J. Rho, S. A. Maier, *Nat. Nanotechnol.* **2020**, *15*, 948.
- [28] B. Zhen, C. W. Hsu, L. Lu, A. D. Stone, M. Soljačić, *Phys. Rev. Lett.* **2014**, *113*, 257401.
- [29] H. M. Doeleman, F. Monticone, W. den Hollander, A. Alù, A. F. Koenderink, *Nat. Photonics* **2018**, *12*, 397.
- [30] B. Wang, W. Liu, M. Zhao, J. Wang, Y. Zhang, A. Chen, F. Guan, X. Liu, L. Shi, J. Zi, *Nat. Photonics* **2020**, *14*, 623.
- [31] X. Cai, J. Wang, M. J. Strain, B. Johnson-Morris, J. Zhu, M. Sorel, J. L. O'Brien, M. G. Thompson, S. Yu, *Science* **2012**, *338*, 363.
- [32] P. Miao, Z. Zhang, J. Sun, W. Walasik, S. Longhi, N. M. Litchinitser, L. Feng, *Science* **2016**, *353*, 464.
- [33] N. C. Zambon, P. St-Jean, M. Milićević, A. Lemaître, A. Harouri, L. L. Gratiot, O. Bleu, D. D. Solnyshkov, G. Malpuech, I. Sagnes, S. Ravets, A. Amo, J. Bloch, *Nat. Photonics* **2019**, *13*, 283.
- [34] Z. Zhang, X. Qiao, B. Midya, K. Liu, J. Sun, T. Wu, W. Liu, R. Agarwal, J. M. Jornet, S. Longhi, N. M. Litchinitser, L. Feng, *Science* **2020**, *368*, 760.
- [35] B. Chen, Y. Wei, T. Zhao, S. Liu, R. Su, B. Yao, Y. Yu, J. Liu, X. Wang, *Nat. Nanotechnol.* **2021**, *16*, 302.
- [36] H. Kim, J. Park, S.-W. Cho, S.-Y. Lee, M. Kang, B. Lee, *Nano Lett.* **2010**, *10*, 529.
- [37] G. Spector, D. Kilbane, A. K. Mahro, B. Frank, S. Ristok, L. Gal, P. Kahl, D. Podbiel, S. Mathias, H. Giessen, F.-J. M. zu Heringdorf, M. Orenstein, M. Aeschlimann, *Science* **2017**, *355*, 1187.
- [38] P. Genevet, J. Lin, M. A. Kats, F. Capasso, *Nat. Commun.* **2012**, *3*, 1278.
- [39] S. Mei, K. Huang, H. Liu, F. Qin, M. Q. Mehmood, Z. Xu, M. Hong, D. Zhang, J. Teng, A. Danner, C.-W. Qiu, *Nanoscale* **2015**, *8*, 2227.
- [40] H. Ren, X. Li, Q. Zhang, M. Gu, *Science* **2016**, *352*, 805.
- [41] Z. Yue, H. Ren, S. Wei, J. Lin, M. Gu, *Nat. Commun.* **2018**, *9*, 4413.
- [42] F. Feng, G. Si, C. Min, X. Yuan, M. Somekh, *Light: Sci. Appl.* **2020**, *9*, 95.
- [43] H. Ren, X. Wang, C. Li, C. He, Y. Wang, A. Pan, S. A. Maier, *Nano Lett.* **2021**, *21*, 6220.
- [44] Z. Ji, W. Liu, S. Krylyuk, X. Fan, Z. Zhang, A. Pan, L. Feng, A. Davydov, R. Agarwal, *Science* **2020**, *368*, 763.
- [45] S. A. Maier, *Plasmonics: Fundamentals and Applications*, Springer, New York **2007**.
- [46] S. Sun, Q. He, J. Hao, S. Xiao, L. Zhou, *Adv. Opt. Photonics* **2019**, *11*, 380.
- [47] L. Novotny, B. Hecht, *Principles of Nano-Optics*, Cambridge University Press, New York **2006**.
- [48] A. Pors, M. G. Nielsen, R. L. Eriksen, S. I. Bozhevolnyi, *Nano Lett.* **2013**, *13*, 829.
- [49] F. Ding, Y. Yang, R. A. Deshpande, S. I. Bozhevolnyi, *Nanophotonics* **2018**, *7*, 1129.
- [50] B. E. A. Saleh, M. C. Teich, *Fundamentals of Photonics*, 3rd Ed., John Wiley & Sons, New York **2019**, pp. 209–255.
- [51] S. Pancharatnam, *Proc. Indian Acad. Sci., Sect. A* **1956**, *44*, 398.
- [52] M. V. Berry, *Proc. R. Soc. London, Ser. A* **1984**, *392*, 45.
- [53] M. Decker, I. Staude, M. Falkner, J. Dominguez, D. N. Neshev, I. Brener, T. Pertsch, Y. S. Kivshar, *Adv. Opt. Mater.* **2015**, *3*, 813.
- [54] A. Arbabi, R. M. Briggs, Y. Horie, M. Bagheri, A. Faraon, *Opt. Express* **2015**, *23*, 33310.
- [55] M. Khorasaninejad, Z. Shi, A. Y. Zhu, W. T. Chen, V. Sanjeev, A. Zaidi, F. Capasso, *Nano Lett.* **2017**, *17*, 1819.
- [56] D. Lin, P. Fan, E. Hasman, M. L. Brongersma, *Science* **2014**, *345*, 298.
- [57] M. Khorasaninejad, W. T. Chen, R. C. Devlin, J. Oh, A. Y. Zhu, F. Capasso, *Science* **2016**, *352*, 1190.
- [58] Z. Bomzon, G. Biener, V. Kleiner, E. Hasman, *Opt. Lett.* **2002**, *27*, 1141.
- [59] A. Arbabi, Y. Horie, M. Bagheri, A. Faraon, *Nat. Nanotechnol.* **2015**, *10*, 937.
- [60] J. P. B. Mueller, N. A. Rubin, R. C. Devlin, B. Groever, F. Capasso, *Phys. Rev. Lett.* **2017**, *118*, 113901.
- [61] I. Nape, B. Sephton, Y.-W. Huang, A. Vallés, C.-W. Qiu, A. Ambrosio, F. Capasso, A. Forbes, *APL Photonics* **2020**, *5*, 070802.
- [62] P. Huo, C. Zhang, W. Zhu, M. Liu, S. Zhang, S. Zhang, L. Chen, H. J. Lezec, A. Agrawal, Y. Lu, T. Xu, *Nano Lett.* **2020**, *20*, 2791.
- [63] Y. Montelongo, J. O. Tenorio-Pearl, W. I. Milne, T. D. Wilkinson, *Nano Lett.* **2014**, *14*, 294.
- [64] D. Wen, F. Yue, G. Li, G. Zheng, K. Chan, S. Chen, M. Chen, K. F. Li, P. W. H. Wong, K. W. Cheah, E. Y. B. Pun, S. Zhang, X. Chen, *Nat. Commun.* **2015**, *6*, 8241.
- [65] Y.-W. Huang, W. T. Chen, W.-Y. Tsai, P. C. Wu, C.-M. Wang, G. Sun, D. P. Tsai, *Nano Lett.* **2015**, *15*, 3122.
- [66] X. Li, L. Chen, Y. Li, X. Zhang, M. Pu, Z. Zhao, X. Ma, Y. Wang, M. Hong, X. Luo, *Sci. Adv.* **2016**, *2*, e1601102.
- [67] S. M. Kamali, E. Arbabi, A. Arbabi, Y. Horie, M. Faraji-Dana, A. Faraon, *Phys. Rev. X* **2017**, *7*, 041056.
- [68] M. Piccardo, V. Ginis, A. Forbes, S. Mahler, A. A. Friesem, N. Davidson, H. Ren, A. H. Dorrah, F. Capasso, F. T. Dullo, B. S. Ahluwalia, A. Ambrosio, S. Gigan, N. Treps, M. Hiekkämäki, R. Fickler, M. Kues, D. Moss, R. Morandotti, J. Riemensberger, T. J. Kippenberg, J. Faist, G. Scalari, N. Picqué, T. W. Hänsch, G. Cerullo, C. Manzoni, L. A. Lugiato, M. Brambilla, L. Columbo, et al., *J. Opt.* **2022**, *24*, 013001.
- [69] S. Zhang, P. Huo, W. Zhu, C. Zhang, P. Chen, M. Liu, L. Chen, H. J. Lezec, A. Agrawal, Y. Lu, T. Xu, *Laser Photonics Rev.* **2020**, *14*, 2000062.
- [70] D. Song, V. Paltoglou, S. Liu, Y. Zhu, D. Gallardo, L. Tang, J. Xu, M. Ablowitz, N. K. Efremidis, Z. Chen, *Nat. Commun.* **2015**, *6*, 6272.
- [71] C. W. Hsu, B. Zhen, A. D. Stone, J. D. Joannopoulos, M. Soljačić, *Nat. Rev. Mater.* **2016**, *1*, 16048.
- [72] C. Huang, C. Zhang, S. Xiao, Y. Wang, Y. Fan, Y. Liu, N. Zhang, G. Qu, H. Ji, J. Han, L. Ge, Y. Kivshar, Q. Song, *Science* **2020**, *367*, 1018.
- [73] X. Liu, S. Xia, E. Jajtić, D. Song, D. Li, L. Tang, D. Leykam, J. Xu, H. Buljan, Z. Chen, *Nat. Commun.* **2020**, *11*, 1586.
- [74] Z.-Q. Yang, Z.-K. Shao, H.-Z. Chen, X.-R. Mao, R.-M. Ma, *Phys. Rev. Lett.* **2020**, *125*, 013903.
- [75] M. J. Strain, X. Cai, J. Wang, J. Zhu, D. B. Phillips, L. Chen, M. Lopez-Garcia, J. L. O'Brien, M. G. Thompson, M. Sorel, S. Yu, *Nat. Commun.* **2014**, *5*, 4856.
- [76] Z. Shao, J. Zhu, Y. Chen, Y. Zhang, S. Yu, *Nat. Commun.* **2018**, *9*, 926.
- [77] M. Erhard, R. Fickler, M. Krenn, A. Zeilinger, *Light: Sci. Appl.* **2018**, *7*, 17146.
- [78] A. Mair, A. Vaziri, G. Weihs, A. Zeilinger, *Nature* **2001**, *412*, 313.
- [79] E. Ozbay, *Science* **2006**, *311*, 189.

- [80] D. K. Gramotnev, S. I. Bozhevolnyi, *Nat. Photonics* **2010**, *4*, 83.
- [81] X. Zhao, X. Feng, F. Liu, K. Cui, W. Zhang, Y. Huang, *ACS Photonics* **2020**, *7*, 212.
- [82] H. Ren, M. Gu, *Laser Photonics Rev.* **2018**, *12*, 1700255.
- [83] M. Zhang, H. Ren, X. Ouyang, M. Jiang, Y. Lu, Y. Hu, S. Fu, Z. Li, Z. Chen, B.-O. Guan, Y. Cao, X. Li, *ACS Photonics* **2021**, *8*, 1169.
- [84] J. Chen, X. Chen, T. Li, S. Zhu, *Laser Photonics Rev.* **2018**, *12*, 1700331.
- [85] P. D. Pietro, M. Ortolani, O. Limaj, A. D. Gaspare, V. Giliberti, F. Giorgianni, M. Brahlek, N. Bansal, N. Koirala, S. Oh, P. Calvani, S. Lupi, *Nat. Nanotechnol.* **2013**, *8*, 556.
- [86] Z. Yue, B. Cai, L. Wang, X. Wang, M. Gu, *Sci. Adv.* **2016**, *2*, e1501536.
- [87] D. Pesin, A. H. MacDonald, *Nat. Mater.* **2012**, *11*, 409.
- [88] Y. Yan, C. Zhang, J. Y. Zheng, J. Yao, Y. S. Zhao, *Adv. Mater.* **2012**, *24*, 5681.
- [89] H. Yang, V. Khayrudinov, V. Dhaka, H. Jiang, A. Autere, H. Lipsanen, Z. Sun, H. Jussila, *Sci. Adv.* **2018**, *4*, eaar7954.
- [90] J. Lin, J. P. B. Mueller, Q. Wang, G. Yuan, N. Antoniou, X.-C. Yuan, F. Capasso, *Science* **2013**, *340*, 331.
- [91] M. Plidschun, H. Ren, J. Kim, R. Förster, S. A. Maier, M. A. Schmidt, *Light: Sci. Appl.* **2021**, *10*, 57.
- [92] W. Hadibrata, H. Wei, S. Krishnaswamy, K. Aydin, *Nano Lett.* **2021**, *21*, 2422.
- [93] D. Chanda, K. Shigeta, S. Gupta, T. Cain, A. Carlson, A. Mihi, A. J. Baca, G. R. Bogart, P. Braun, J. A. Rogers, *Nat. Nanotechnol.* **2011**, *6*, 402.
- [94] N. Li, Y. H. Fu, Y. Dong, T. Hu, Z. Xu, Q. Zhong, D. Li, K. H. Lai, S. Zhu, Q. Lin, Y. Gu, N. Singh, *Nanophotonics* **2019**, *8*, 1855.
- [95] G. Yoon, K. Kim, D. Huh, H. Lee, J. Rho, *Nat. Commun.* **2020**, *11*, 2268.
- [96] N. Hjjaj, I. Larkin, E. W. Rosenthal, S. Zahedpour, J. K. Wahlstrand, H. M. Milchberg, *Phys. Rev. X* **2016**, *6*, 031037.
- [97] A. Chong, C. Wan, J. Chen, Q. Zhan, *Nat. Photonics* **2020**, *14*, 350.
- [98] L. Rego, K. M. Dorney, N. J. Brooks, Q. L. Nguyen, C.-T. Liao, J. S. Román, D. E. Couch, A. Liu, E. Pisanty, M. Lewenstein, L. Plaja, H. C. Kapteyn, M. M. Murnane, C. Hernández-García, *Science* **2019**, *364*, eaaw9486.
- [99] S.-Q. Li, X. Xu, R. M. Veetil, V. Valuckas, R. Paniagua-Domínguez, A. I. Kuznetsov, *Science* **2019**, *364*, 1087.
- [100] P. Kepič, F. Ligmajer, M. Hrtoň, H. Ren, L. S. de Menezes, S. A. Maier, T. Šikola, *ACS Photonics* **2021**, *8*, 1048.
- [101] P. Genevet, F. Capasso, F. Aieta, M. Khorasaninejad, R. Devlin, *Optica* **2017**, *4*, 139.
- [102] Y. Shen, X. Wang, Z. Xie, C. Min, X. Fu, Q. Liu, M. Gong, X. Yuan, *Light: Sci. Appl.* **2019**, *8*, 90.
- [103] C. Li, S. A. Maier, H. Ren, *Chin. Opt.* **2021**, *14*, 792.
- [104] Vortex Photonics, <https://www.vortex-photonics.de/> (accessed: January 2022).
- [105] R. Fickler, R. Lapkiewicz, M. Huber, M. P. J. Lavery, M. J. Padgett, A. Zeilinger, *Nat. Commun.* **2014**, *5*, 4502.



Haoran Ren gained a Ph.D. in 2017 from Swinburne University of Technology in Australia. From October 2016, he was a Postdoc at RMIT University. In 2018, he took a Victoria Fellowship to visit the National Centre for Scientific Research in France for three months. In January 2019, he was awarded a Humboldt Research Fellowship to relocate his research to Ludwig Maximilian University of Munich in Germany. He was thereafter awarded a DECRA Fellowship from the Australian Research Council and a Macquarie University Research Fellowship from Macquarie University, through which he moved his research back to Australia in December 2020.



Stefan A. Maier currently holds the Chair in Hybrid Nanosystems at LMU Munich and the Lee Lucas Chair in Physics at the Imperial College London. He graduated with a Ph.D. in applied physics from Caltech, before taking up a Lecturer position at the University of Bath. In 2008, he moved to Imperial College London, where he stayed on full-time until 2018. He is a Fellow of the OSA and the Institute of Physics.